Composites: Part A 61 (2014) 23–32

Contents lists available at ScienceDirect

Composites: Part A

journal homepage: www.elsevier.com/locate/compositesa

A finite element unit-cell method for homogenised mechanical properties of heterogeneous plates

A. Schmitz *, P. Horst

Institute of Aircraft Design and Lightweight Structures, TU Braunschweig, Hermann-Blenk-Strasse 35, 38108 Braunschweig, Germany

ARTICLE INFO

Article history:
Received 2 July 2013
Received in revised form 16 January 2014
Accepted 26 January 2014
Available online 4 February 2014

Keywords:
B. Transverse cracking
C. Finite element analysis (FEA)
C. Computational modelling
D. Mechanical testing

ABSTRACT

This paper presents a 3D unit-cell approach which enables estimations of all bending, in-plane and coupling properties in the sense of the classical laminated plate theory for heterogeneous plates. For this reason, periodic boundary conditions which simultaneously allow in-plane as well as bending/twisting deformation modes are introduced. In contrast to existing approaches, the 3D unit-cell is connected with the macroscopic plate theory by means of prescribed loads and the extraction of strains/curvatures. Novel bending experiments at large curvatures of E-glass-fibre/epoxy cross-ply laminate with cracking outer ply at the bending tension side are conducted. Subsequently, numerical results are validated by comparing them to the measured bending stiffness degradation. Further, the effects of the single-sided transverse cracks on relevant stiffness properties are computed.

1. Introduction

There is a wide interest in analysing and understanding the mechanical behaviour of complex thin engineering structures. Hence, this paper focuses on the mechanical characterisation of heterogeneous plates. Regarding the field of fibre-reinforced composites, it can be stated that the presented approach still performs beyond the possibilities of methods based on ply-level homogenisation. Generally, heterogeneities are not restricted to a single ply. Hence, a finite element unit-cell method is introduced which extracts in-plane as well as in-plane/bending coupling and bending properties in the sense of the classical laminated plate theory [1]. Useful applications are analyses of the impact on overall properties of damages like delaminations and cracks or morphing skins (mostly being highly heterogeneous).

However, up to a certain degree of heterogeneity, sophisticated structural theories exist (e.g. for layered composite laminates [2], sandwich structures [3], honeycomb structures [4,5] or corrugated panels [6,7]). In case of more complex structural configurations, computational homogenisation techniques promise satisfying results.

Computational homogenisation is characterised by analysing a representative part of a structure, the representative volume element, mostly modelled within the finite element method. Then, a load is imposed together with specific boundary conditions [8]. Terada et al. [9] shows that periodic boundary conditions superiorly describe the mechanical behaviour of the unit-cell compared to pure displacement or traction boundaries. Finally, homogenised mechanical quantities are extracted. Currently, two different frameworks can be distinguished.

Firstly, there is the multi-scale finite element method [10] which solves a second boundary value problem (a representative unit-cell) instead of a constitutive relation. Herein, the averaged mechanical response (averaged stress and tangent tensors) is transferred from the unit-cell back to the macro-scale boundary value problem. Although this is of high computational costs, it is a proven method for analysing multiphase materials. As the unit-cell represents the material behaviour at a certain material point, this concept is only valid as long as the deformation gradient is approximately constant over the whole unit-cell. Thus, bending and twisting deformation modes of the unit-cell itself cannot be analysed. In order to face this deficiency, Kouznetsova et al. [11] present a second-order computational homogenisation framework. Further increase of the gradient of the deformation gradient at the scale of the modelled heterogeneity within the unit-cell is treated by Coenen et al. [12] using a shell formulation at the macro-scale and 3D continuum mechanics for the unit-cell. All these multi-scale approaches prescribe macroscopic deformations, because the unit-cell replaces the constitutive relation and the displacements are the primary variables within the finite element method.

Secondly, in case of linear elastic unit-cell constituent materials and small strains and displacements, computational homogenisation can also be performed with omitted macro-scale boundary

* Corresponding author. Tel.: +49 (0)531 391 9910.
E-mail address: a.schmitz@tu-bs.de (A. Schmitz).

http://dx.doi.org/10.1016/j.compositesa.2014.01.014
1359-835X/

value problem. Herein, representative stiffness properties are independent of the actual deformation state and can thus be derived prior analysing the macro-level boundary value problem. The extraction is conducted using multiple particular loadcases together with the principle of superposition. Those approaches are often settled in the field of fibre-reinforced composites. In contrast to the multi-scale finite element framework, prescribed macroscopic stress states are mostly preferred [13–16]. Generally, unit-cells capturing macroscopic bending modes are rare. For example Jiang [17] presents a representative section of wire strand and Ju et al. [18] analyse coronary stents under pure bending. Both extract a single homogenised bending stiffness. However, note that all bending formulations use prescribed macroscopic displacements.

The goal of this paper is the formulation of a 3D unit-cell from which, for the first time, all (in-plane, bending and in-plane/bending coupling) stiffness entries of the classical laminated plate theory are extracted. Thus, a 3D representative structure is homogenised as anisotropic Kirchhoff–Love plate. The classical laminated plate theory is chosen as representative theory as this is a common approach when dealing with orthotropic composite plates and at least some stiffness entries can be measured directly. In the presented approach the whole geometric extension of the plate in thickness-direction is modelled, hence, the unit-cell behaves only in-plane periodically. As the unit-cell spans over all laminate layers, homogenisation is typically done at the scale of the laminate. Hence, this type of unit-cell is further named representative structure element (RSE).

With respect to linear elasticity, identical results are obtained if macroscopic forces/moments are prescribed and macroscopic strains/curvatures extracted or vice versa. However, in contrast to unit-cells restricted to in-plane loads the unknown lateral poisson contraction displacements would have to be taken into account if curvatures are to be prescribed to a 3D unit-cell. Additionally, all initially unknown and generally independent elastic neutral planes, namely for bending the x-axis, y-axis and for twisting would also be needed for imposing the boundary conditions. Hence, in order to achieve optimal mechanical unit-cell behaviour, the presented approach uses prescribed macroscopic forces/moments. As benefit, less assumptions regarding the kinematic of the bending cross-section must be made. Namely, there is no need to add any assumptions regarding the angles between cross-sections and bending neutral planes.

The first part of this paper focusses on the formulation of the RSE. The second part (as one possible application) applies the RSE approach to an E-glass-fibre/epoxy cross-ply laminate with outer, single-sided transverse cracks (due to bending). As the mechanical response of the RSE is represented by the classical laminated plate theory discrete singularities are smeared at the scale of the laminate. This is known as continuum damage mechanics approach, which has first been applied to cracked composite plies by Talreja [19]. Transverse ply-cracking is widely investigated for in-plane loads, see the review by Berthelot [20], but rarely due to bending. The few publications deal with 2D approaches to calculate single bending properties [21–23]. Additionally, bending experiments are conducted in order to validate the RSE capabilities in terms of the novel estimation of bending/twisting and coupling properties. In order to present new experimental data, the bending stiffness degradation due to transverse cracking caused by pure bending is recorded. A specially designed bending fixture creating large and almost pure bending deformations is used. Hence, high crack-densities due to bending along with a large cross-section fraction being damaged are generated.

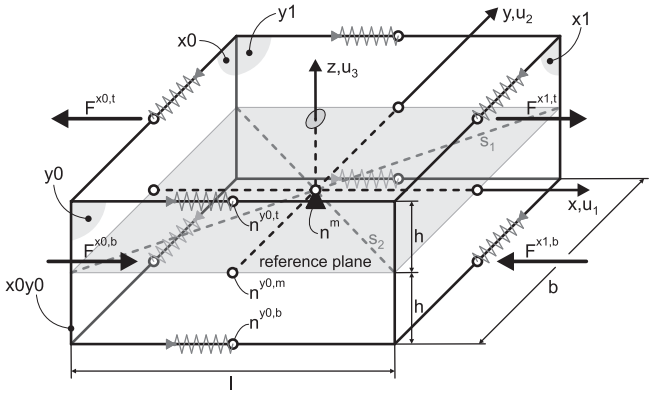

Fig. 1. RSE notations and dimensions. Naming conventions for specific nodes are exemplarily given for face y0. Jagged lines indicate the linear springs.

2. Formulation of the unit-cell

This section presents the theoretical background of the unit-cell formulation. For the first time, all stiffness properties of the classical laminated plate theory are directly extracted for an arbitrary heterogeneous sheet. All analyses are conducted with the finite element code ABAQUS®.

2.1. Periodic boundary conditions

When periodicity is assumed, opposite faces and edges are intended to deform identically. Hence, from the mechanical point of view the cut boundaries of the unit-cell are connected to an infinite expanse of identical repeated unit-cells under identical loading as the modelled unit-cell. A sketch of the rectangular RSE unit-cell with used notations is given in Fig. 1. The implementation of periodic boundary conditions requires equally located nodes on opposite faces and edges. With this requirement, one constraint equation is formulated for each opposite node pair and incorporated into the finite element framework via multiple point constraints. In detail, the displacements of both nodes of each node pair are constrained relatively to each other and to the displacements of the loaded nodes. This coupling of opposite node pairs allows a certain superimposed fluctuation field resulting from a heterogeneous structure. There are eight nodes located at the centre of each top and bottom edge (e.g. node $n^{y0,b}$ and $n^{y0,t}$ in Fig. 1) which are loaded with discrete forces.

The central idea of this unit-cell is to apply multiple loadcases with only one non-zero flux and to extract the corresponding deformations in the sense of a 2D Kirchhoff–Love plate. Considering anisotropic behaviour, all six strains and curvatures may become non-zero for each loadcase. Consequently, the boundary conditions must ensure free deformability. The presented boundary conditions fulfil this requirement by exclusively implementing translational symmetry. Namely, as stated by Li and Zou [24], other symmetries like reflection and rotation typically fail to maintain the sense of non-direct shear stresses and strains. However, one assumption must be made. Only the degrees of freedom in x- and y-direction (displacements u_α with $\alpha = 1, 2$) are incorporated into the periodicity constraints Eqs. (1)–(4) because the unit-cell represents the whole plate in z-direction and thus it can be assumed that the x- and y-displacements are dominantly responsible for the in-plane mechanical behaviour. Although strict periodicity would also require to incorporate the degree of freedom in thickness direction u_3, it must be excluded in order to permit the twisting deformation mode (as u_3 behaves antisymmetrically in this case).

The periodicity constraints in x-direction are given for every associated node pair i located at the faces x0 and x1 with the normalised thickness-coordinate $\zeta^i = z^i/h$ by

$$u_\alpha^{x1,i} = u_\alpha^{x0,i} + \frac{1}{2}\left(1-\zeta^i\right)\left(u_\alpha^{x1,b} - u_\alpha^{x0,b}\right) + \frac{1}{2}\left(\zeta^i+1\right)\left(u_\alpha^{x1,t} - u_\alpha^{x0,t}\right) \quad (1)$$

and similarly in y-direction by

$$u_\alpha^{y1,i} = u_\alpha^{y0,i} + \frac{1}{2}\left(1-\zeta^i\right)\left(u_\alpha^{y1,b} - u_\alpha^{y0,b}\right) + \frac{1}{2}\left(\zeta^i+1\right)\left(u_\alpha^{y1,t} - u_\alpha^{y0,t}\right). \quad (2)$$

In order to avoid over-determined nodes, all loaded nodes are excluded from these constraints. The same holds for all nodes located at the vertical edges which are shared by two faces. However, these edge-nodes are connected as well to maintain diagonal periodicity, too. Precisely, the edges x0y0 and x1y1 are constrained via

$$u_\alpha^{x1y1,i} = u_\alpha^{x0y0,i} + \frac{1}{2}\left(1-\zeta^i\right)\left(u_\alpha^{x1,b} - u_\alpha^{x0,b}\right) + \frac{1}{2}\left(\zeta^i+1\right)\left(u_\alpha^{x1,t} - u_\alpha^{x0,t}\right) + \frac{1}{2}\left(1-\zeta^i\right)\left(u_\alpha^{y1,b} - u_\alpha^{y0,b}\right) + \frac{1}{2}\left(\zeta^i+1\right)\left(u_\alpha^{y1,t} - u_\alpha^{y0,t}\right) \quad (3)$$

and the edges x0y1 and x1y0 via

$$u_\alpha^{x1y0,i} = u_\alpha^{x0y1,i} + \frac{1}{2}\left(1-\zeta^i\right)\left(u_\alpha^{x1,b} - u_\alpha^{x0,b}\right) + \frac{1}{2}\left(\zeta^i+1\right)\left(u_\alpha^{x1,t} - u_\alpha^{x0,t}\right) + \frac{1}{2}\left(1-\zeta^i\right)\left(u_\alpha^{y1,b} - u_\alpha^{y0,b}\right) + \frac{1}{2}\left(\zeta^i+1\right)\left(u_\alpha^{y1,t} - u_\alpha^{y0,t}\right). \quad (4)$$

At the upper and lower face zero-traction boundary conditions are imposed. Note, that the in-plane dimensions of the RSE are generally arbitrary and thus only depend on the dimensions of the representative structure.

2.2. Rigid body constraints

The RSE approach prescribes forces and requires free deformability. Hence, the suppression of rigid body motion must be paid particular attention. Without bending and twisting deformation modes rigid body translation and rotation can be suppressed via rigid single point constraints [14]. However, having simultaneously to account for all deformation modes together with the chosen loadcases (Fig. 2) this practice becomes impossible as there are no exploitable symmetries of the displacement field in case of a fully coupled plate. Thus, only the middle node n^m is fixed in all spatial directions which completely avoids rigid body translation. In order to allow the RSE to deform freely under load and simultaneously suppress rigid body rotation, weak linear springs are connected to the eight loaded nodes, cp. Fig. 1. The compliance of these springs is chosen at least 10^5 magnitudes higher than the most compliant RSE constituent. Thus, the numerical stability is achieved without affecting the mechanical response.

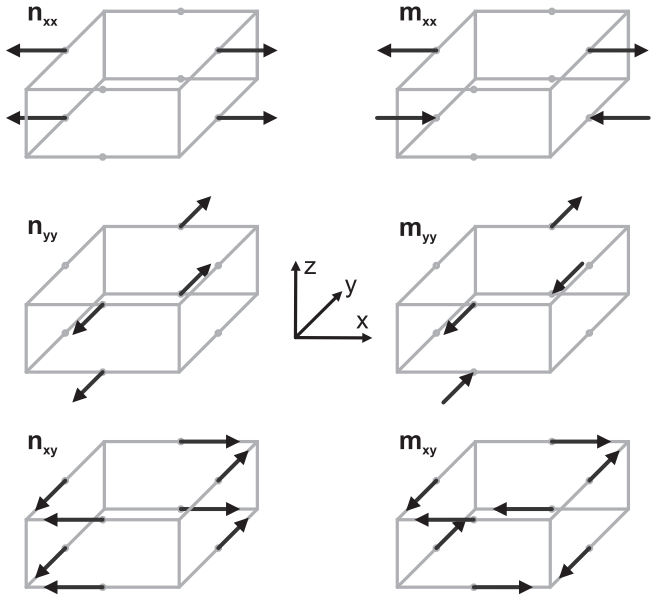

Fig. 2. Schematic view of the six loadcases.

2.3. Representative stiffness properties

The arbitrary flat sheet is represented by the classical laminated plate theory considering all stiffness entries. Hence, the macroscopic constitutive relation reads [1]

$$\begin{Bmatrix} n_{xx} \\ n_{yy} \\ n_{xy} \\ m_{xx} \\ m_{yy} \\ m_{xy} \end{Bmatrix} = \mathbf{ABD} \begin{Bmatrix} \epsilon_{xx} \\ \epsilon_{yy} \\ \epsilon_{xy} \\ \kappa_{xx} \\ \kappa_{yy} \\ \kappa_{xy} \end{Bmatrix}. \quad (5)$$

Herein, $\{\epsilon_{xx}, \epsilon_{yy}, \epsilon_{xy}, \kappa_{xx}, \kappa_{yy}, \kappa_{xy}\}^T$ denote the strains and curvatures and the force and moment fluxes are given by $\{n_{xx}, n_{yy}, n_{xy}, m_{xx}, m_{yy}, m_{xy}\}^T$. All components refer to the plate's reference plane commonly located at the geometric centre in thickness-direction. The relation between fluxes and strains/curvatures is given by

$$\mathbf{ABD} = \begin{bmatrix} A_{11} & A_{12} & A_{13} & B_{11} & B_{12} & B_{13} \\ A_{21} & A_{22} & A_{23} & B_{21} & B_{22} & B_{23} \\ A_{31} & A_{32} & A_{33} & B_{31} & B_{32} & B_{33} \\ B_{11} & B_{12} & B_{13} & D_{11} & D_{12} & D_{13} \\ B_{21} & B_{22} & B_{23} & D_{21} & D_{22} & D_{23} \\ B_{31} & B_{32} & B_{33} & D_{31} & D_{32} & D_{33} \end{bmatrix} \quad (6)$$

where A_{ij} describes the in-plane behaviour, D_{ij} the out-of-plane behaviour and B_{ij} the coupling characteristics. If the RSE is loaded with a single macroscopic flux and the six attendant strains/curvatures are known, all compliance entries in the corresponding column of the $\mathbf{ABD}^{-1}$ matrix, defined by

$$\begin{Bmatrix} \epsilon_{xx} \\ \epsilon_{yy} \\ \epsilon_{xy} \\ \kappa_{xx} \\ \kappa_{yy} \\ \kappa_{xy} \end{Bmatrix} = \mathbf{ABD}^{-1} \begin{Bmatrix} n_{xx} \\ n_{yy} \\ n_{xy} \\ m_{xx} \\ m_{yy} \\ m_{xy} \end{Bmatrix} \quad (7)$$

are determined. Note that this procedure derives every matrix entry separately and therefore is able to account for potential unsymmetrical mechanical response.

Six loadcases are needed to evaluate all **ABD** entries. Every loadcase stresses the unit-cell with a single and distinct macroscopic flux (only one flux in Eq. (7) is non-zero). A sketch of each loading configuration is given in Fig. 2. Thereby, the force magnitudes are always equal within each loadcase. Afterwards, all strains and curvatures are extracted. The intended prescribed fluxes together with the geometric dimensions of the unit-cell determine the

magnitude of the corresponding discrete forces, see Table 1. Herein, the first index denotes the direction of the force and the second the direction of the surface normal the force is acting on.

2.4. Representative strain state

The RSE concept leaves the strain state unknown in advance and determines it after deformation. In order to maintain consistency, strains/curvatures are determined at the geometric reference plane of the unit-cell. Precisely, the curvatures κ_{xx} and κ_{yy} are determined along the deformed x- and y-axis, respectively. The calculation of the twist κ_{xy} is performed along the two diagonals (diagonal s_1 from vertical edge x0y0 to x1y1 and s_2 from x0y1 to x1y0, cp. Fig. 1) of the rectangular reference plane.

The average global curvature of a deformed line segment is calculated via its mean radius r as

$$\kappa = 1/r. \tag{8}$$

This approach shows robust behaviour because the topology of the approximated interpolation function (circle) is exploited. Local curvature courses can also be estimated by calculating local circle radii r^{local} for chosen (local) line segments.

The determination of the circle radii is conducted using a least-square approach which, however, would yield results with emphases on areas with accumulated finite element nodes. In order to overcome this deficiency, equidistant artificial points are generated first. This is conducted by radial basis function interpolation along the crucial lines. This preparation ensures an even least square weighting throughout the unit-cell.

Radial basis functions are well-established for approximating multi-dimensional data, see e.g. the books [25,26], with the benefit that no shape-type or approximation degree must be defined. The approximation of a scalar u over a n-dimensional data field $\mathbf{x}$ with $\mathbf{x} \in \mathcal{R}^n$ denotes

$$u(\mathbf{x}) = \sum_{j=1}^{p} \alpha_j \, \phi(||\mathbf{x} - \mathbf{x}_j||). \tag{9}$$

Herein, the weights α_j are calculated for every sample point j using a linear least square procedure. The radial basis function ϕ is defined at every sample point and only depends on the geometric distance (euclidean norm) $R = ||\mathbf{x} - \mathbf{x}_j||$ from each sample point. In the presented approach a multi-quadratic basis-function

$$\phi(R) = \sqrt{1 + (R/\tau)^2} \tag{10}$$

is chosen due to its more global response. The parameter τ is set to the average distance of the finite element nodes which serve as the sample points. Generally, there are no restrictions of the finite element mesh regarding the strain/curvature estimation as artificial points can be created in the 3D space along the crucial lines via interpolation. Nevertheless, due to improved accuracy and calculation time, finite element nodes are already set along the x- and y-axis and within the reference plane in all following models. This reduces the approximation to the 1D and 2D space, respectively.

Fitting circles to scattered data in the plane is needed in many applications, e.g. computer graphics and visualisation, meteorology, statistics, physics [27–31]. Many algorithms have been developed from which the class of geometric fit approaches promises most accurate results. These algorithms minimise the geometric distance between the circle and the given points in a least square sense which results in the solution of a non-linear problem. Herein, the mathematical task is the determination of the constants A and B (denoting the coordinates of the circle's centre) and the radius r of the circle-equation

$$(s_i - A)^2 + (z_i - B)^2 = r^2 \tag{11}$$

that for all given points (s_i, z_i) with $i = 1, n$ and $n \geqslant 3$ the distances d_i to the resultant circle are minimised. The corresponding functional then reads

$$\mathcal{F}(A, B, r) = \sum_{i=1}^{n} d_i^2 = min. \tag{12}$$

with

$$d_i = \sqrt{(s_i - A)^2 + (z_i - B)^2} - r. \tag{13}$$

In order to solve this non-linear least square problem for the optimal circle parameters A, B and r an initial guess is estimated by solving a linear least square problem first. With the introduction of $\alpha = 2A, \beta = 2B$ and $\gamma = r^2 - A^2 - B^2$ the circle equation becomes linear in the introduced parameters, namely

$$\alpha s_i + \beta z_i + \gamma = s_i^2 + z_i^2. \tag{14}$$

After solving the over-determined system of equations the circle constants are recalculated from the introduced parameters.

Finally, the bending and twisting curvatures are calculated following Eq. (8) as

$$\kappa_{xx} = 1/r_x, \tag{15}$$
$$\kappa_{yy} = 1/r_y, \tag{16}$$
$$\kappa_{xy} = 1/r_{s_1} - 1/r_{s_2}. \tag{17}$$

The radii r_x, r_y are the radii of the deformed x- and y-axis and r_{s_1}, r_{s_2} denote the radii of the two reference plane diagonals s_1 and s_2. The normal strains cannot be extracted by only using the face-nodes at the ends of the x- and y-axis as these change their locations in normal direction also due to a pure bending deformation. Thus, the lengths of these lines after deformation (l_x and l_y) are determined using the calculated global circle radii and the corresponding section-angles (φ_x and φ_y) of the deformed segments via $l_x = r_x \varphi_x$ and $l_y = r_y \varphi_y$. The segment-angles are calculated from the face-node displacements and location of the circle centre. With the undeformed unit-cell lengths (l and b, cp. Fig. 1) the normal strains then become

$$\epsilon_{xx} = (l_x - l)/l, \tag{18}$$
$$\epsilon_{yy} = (l_y - b)/b. \tag{19}$$

The engineering shear strain is estimated with the displacements u_1 of the y-axis face-nodes ($n^{y0,m}$ and $n^{y1,m}$) and u_2 of the x-axes face-nodes ($n^{x0,m}$ and $n^{x1,m}$) as

$$\epsilon_{xy} = tan^{-1}\left(\frac{u_2^{x1,m} - u_2^{x0,m}}{l}\right) + tan^{-1}\left(\frac{u_1^{y1,m} - u_1^{y0,m}}{b}\right). \tag{20}$$

Section 4 shows demonstrative calculations regarding the radial basis function interpolation of finite element nodes, the subsequent generation of equidistant, artificial points and the final estimation of global circle radii.

Table 1
Discrete macroscopic forces for the six loadcases.

Loadcase	Force
$\mathbf{n_{xx}}$	$F_{xx} = n_{xx}\, b/2$
$\mathbf{n_{yy}}$	$F_{yy} = n_{yy}\, l/2$
$\mathbf{n_{xy}}$	$F_{xy} = n_{xy}\, l/2$
	$F_{yx} = n_{xy}\, b/2$
$\mathbf{m_{xx}}$	$F^b_{xx} = m_{xx}\, b/(2h)$
$\mathbf{m_{yy}}$	$F^b_{yy} = m_{yy}\, l/(2h)$
$\mathbf{m_{xy}}$	$F^b_{xy} = m_{xy}\, l/(2h)$
	$F^b_{yx} = m_{xy}\, b/(2h)$

2.5. Unit-cell consistency

At this point the consistency between the unit-cell approach and the classical laminated plate theory is presented. For this reason, a configuration is chosen which can be analysed by both approaches, namely a fully coupled $[0, 30, 60]$ laminate. The corresponding **ABD** matrices are calculated with the RSE and also directly with the classical laminated plate theory. The used material data is given in Table 2. The 3D constitutive relation for each unidirectional composite layer is constructed from these data using the German guideline VDI 2014 [32]. The in-plane dimensions of the RSE are arbitrarily chosen to $l = b = 2.0$ mm. With a ply thickness of $t_{ply} = 0.42$ mm the height becomes $2h = 1.26$ mm. The magnitude of the prescribed fluxes is chosen to generate a strain/curvature state of approximately $\epsilon_{ij} \approx 0.1\%$ and $\kappa_{ij} \approx 1.5\ \mathrm{m}^{-1}$ in order to keep the deformations linear. The RSE is meshed with quadratic, 3D continuum elements with two elements per layer in thickness-direction. The in-plane resolution is adopted to receive approximately equal element edge-lengths. With those settings the RSE solution yields

$$\mathbf{ABD}^{\mathrm{RSE}} = \begin{bmatrix} 36313.1 & 9949.5 & 5828.9 & -5406.9 & 1157.4 & 561.7 \\ 9915.8 & 22858.9 & 5820.2 & 1157.7 & 3081.2 & 1875.9 \\ 5827.5 & 5833.7 & 9827.9 & 560.0 & 1889.1 & 1146.0 \\ -5380.4 & 1157.8 & 563.2 & 4781.5 & 1156.2 & 318.8 \\ 1152.5 & 3085.8 & 1888.1 & 1156.3 & 3387.3 & 874.3 \\ 556.9 & 1887.8 & 1151.0 & 321.4 & 879.1 & 1133.3 \end{bmatrix} \tag{21}$$

with units $[\mathbf{A}] = \mathrm{N/mm}$, $[\mathbf{D}] = \mathrm{Nmm}$ and $[\mathbf{B}] = \mathrm{N}$. Although the laminate behaviour is symmetric (symmetric **ABD** matrix), the RSE solution does not show exactly equal values as every entry is estimated separately. However, if a symmetric stiffness matrix can be ensured the upper and lower triangle matrix might be averaged. In order to quantify the performance of the presented approach, the deviations from the classical laminated plate theory (CLT) are computed as

$$\Delta ABD_{ij} = \left(ABD_{ij}^{\mathrm{RSE}} - ABD_{ij}^{\mathrm{CLT}}\right) / ABD_{ij}^{\mathrm{CLT}} \tag{22}$$

giving

$$\Delta\mathbf{ABD} = \begin{bmatrix} -0.05 & 0.17 & -0.02 & 0.24 & 0.40 & 0.53 \\ -0.17 & -0.03 & -0.17 & 0.42 & -0.23 & -0.73 \\ -0.04 & 0.06 & -0.04 & 0.22 & -0.04 & -0.59 \\ -0.25 & 0.43 & 0.80 & 0.24 & 0.30 & -0.48 \\ -0.02 & -0.08 & -0.09 & 0.31 & 0.08 & -0.59 \\ -0.33 & -0.11 & -0.16 & 0.31 & -0.04 & -0.53 \end{bmatrix} \%. \tag{23}$$

Negative deviations denote smaller values obtained from the RSE solution compared to the analytical one and vice versa. Obviously, the RSE solution mostly underestimates the analytical result although never exceeding a deviation of $\pm 1\%$. Thus, good RSE performance and as well consistency between RSE approach and macro-theory is demonstrated.

Table 2
Material data.

E_m	3400	MPa	E_f	80700	MPa
ν_m	0.38	–	ν_f	0.22	–
t_{ply}	0.42	mm	V_f	51	%

3. Material and methods

The presented RSE approach is advantageous if large heterogeneities like cracks must be considered. Therefore, appropriate validation bending experiments of a cross-ply laminate under static degradation due to transverse cracks are conducted. Separate emphasis is given to the evaluation of the transverse crack-density.

3.1. Material

For optimal damage detection E-glass-fibre rovings Owens Corning OC-111A (1200 tex) with subsequent resin transfer moulding of epoxy resin/hardener Momentive RIM135/RIMH137 are used. Due to the absence of any stitching yarn completely transparent samples are obtained, see Fig. 3(c) and Fig. 5. The samples are cut using a diamond saw. The material data of the manufactured laminate are given in Table 2 and the laminate stacking is $[90, 0]_s$ with constant ply-thickness.

3.2. Bending experiments

The goal of the bending experiments is to receive a relation between the crack-density in the outer, tensioned 90°-ply and the corresponding bending stiffness. Standard bending tests (three- and four-point bending) accurately estimate the initial bending stiffness for small deflections. In order to extend this bending

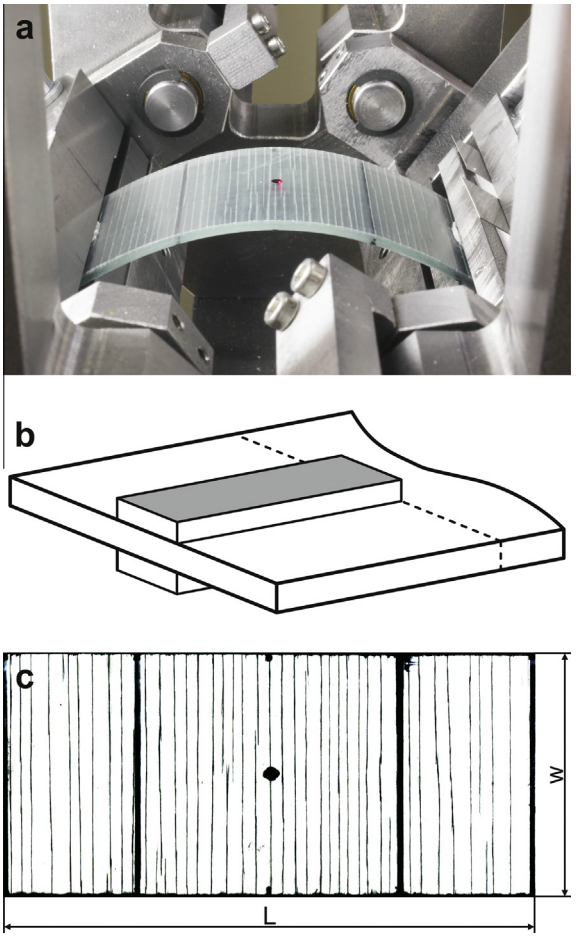

Fig. 3. Large bending device. (a) A bent sample, (b) a detailed view of the clamping condition and (c) a transmitted light scan of a damaged sample (area between the clamps). (For interpretation of the references to colour in this figure legend, the reader is referred to the web version of this article.)

range, a test setup has been constructed, see Fig. 3(a), which can create almost pure bending up to curvatures of 35 m^{-1}. The setup constrains the horizontal distance between the clamped ends of a sample and simultaneously the corresponding angle. The damage-zone between the clamps is $L = 60$ mm and the nominal sample width is $w = 28$ mm, see Fig. 3(c). A detailed description is given in Schmitz and Horst [33].

However, it can be stated that the kinematics in terms of clamp position and corresponding bending angle deviates from a pure bending state by less than 0.2% within the whole curvature range. In contrast, the clamping conditions disturb a constant curvature course and thus must be paid attention. If the sample is completely clamped over its whole width, the bending stiffness will rise towards the clamps because lateral contractions are constrained. Hence, the local curvature will increase around the unconstrained sample centre compared to the constrained sides. Thus, equal strain states along the sample (including the clamped areas) are desirable. In case of large sample width a plain strain state prevails at the bended middle section as well as within the clamps. This configuration is chosen by Boers et al. [34] and Yoshida et al. [35] for large bending experiments. In order to circumvent large sample width and thus maintain convenient dimensions, a plain stress state in width direction is aspired. For this reason, samples are only clamped at their centre in width-direction using compliant foundations (6 mm wide and 0.1 mm thick), cp. Fig. 3(b). This allows anticlastic bending inside the clamps, too. The impact of the boundary condition is measured and presented in Fig. 4. Herein, an unidirectional (25.11 mm wide and 1.26 mm thick) specimen equipped with four strain gauges (Fig. 4(a)) is bent with clamped ends (Fig. 4(b)) and with compliant foundations (Fig. 4(c)). In both cases the strain distribution is symmetric and the strain/curvature behaviour is almost linear. Obviously, the compliant foundation considerably reduces the clamping constraint. However, the tested samples still show slightly decreasing crack-densities towards the clamps. At this point it can be stated that the clamping conditions primarily effect the quality of the bending state. Note, that lateral contraction problems significantly decrease for materials with approximately similar plain stress and strain effective bending moduli, hence for extremely orthotropic samples.

The experiment is structured as follows. The initial bending stiffness is determined in a standard three-point bending test. Thereby, the distance between the outer supports equals the damage-zone L of the large bending fixture and the loading directions are identical (cracks at tension side). Transverse cracks are detected by transmitted light scanning. After recording the unloaded condition, multiple sequences with increasing curvature of a damage cycle (large bending), estimation of the initial bending stiffness (three-point bending) and detection of the corresponding damage state (transmitted light scanning) are conducted.

3.3. Damage evaluation

When loading fibre-reinforced plastics, the first damage which makes sense to describe by a macroscopic fracture model is transverse micro-cracking. Earlier diffuse damages as fibre/matrix debonding and micro-voids are preferably modelled within a continuum mechanics framework. Also in static loading conditions transverse cracks cause delaminations at their crack tips at high loads [20,36]. The intention during the damage cycles is neither to obtain transverse cracks at the pressure side, nor crack-tip delamination.

Although the initiation of transverse micro-cracks is a stochastic phenomenon, cross-ply laminates show an uniform cracking scenario. Herein, the crack-density converges towards an upper limit at high load levels, see e.g. [37,38] for cross-ply laminates

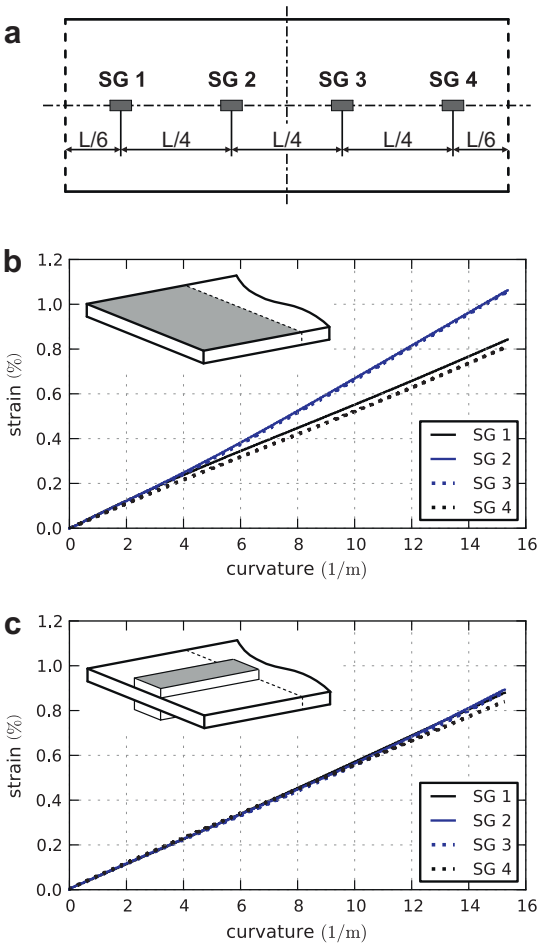

Fig. 4. Large bending strain distributions. An unidirectional sample is equipped with four strain gauges (a) and tested with completely clamped ends (b) and with centred compliant foundations (c). (For interpretation of the references to colour in this figure legend, the reader is referred to the web version of this article.)

under tension. For specimens with relatively thick plies it is observed that transverse cracks mostly initiate at the edges (especially during fatigue loading), immediately extend over the ply-thickness and rapidly grow in the transverse direction [39]. Those phenomena can be observed for the conducted bending experiments, too. Most cracks extend straight over the whole specimen width. However, simultaneously initiated cracks at longitudinally equal and opposite locations restrain each other's expansion after their crack-tips have been overlapped. The same holds for two closely initiated cracks at the same edge. Both scenarios (Fig. 5) create relatively stable partial cracks. Thus, the recorded crack-density ρ is subdivided into complete, straight cracks $\bar{\rho}$ (dashed lines in Fig. 5) and partial cracks ρ_{partial} (solid lines in Fig. 5) giving

$$\rho = \bar{\rho} + \rho_{\text{partial}}. \tag{24}$$

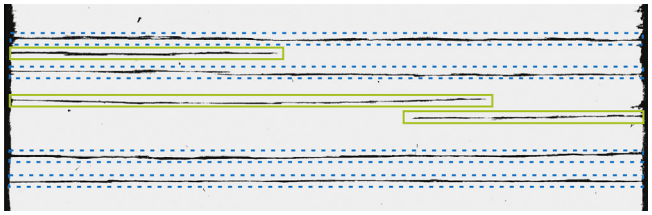

Fig. 5. Exemplary section showing complete (dashed lines) and partial (solid lines) transverse cracks. (For interpretation of the references to colour in this figure legend, the reader is referred to the web version of this article.)

Herein, the crack-density of complete cracks is defined as $\bar{\rho} = \bar{n}/L$ with $\bar{n}$ being the number of complete cracks within the observed damaged sample length L. Similarly, the partial crack-density is defined as $\rho_{\text{partial}} = n_{\text{partial}}/L$ with the number of partial cracks

$$n_{\text{partial}} = \frac{1}{w}\sum_{i=1}^{N_{\text{partial}}} l_i \tag{25}$$

normalised with the sample width w. Note, that this (pseudo) number of partial cracks generally is an odd number. The length of the ith partial crack is denoted by l_i and the absolute (even) number of available partial cracks by N_{partial}.

3.4. Bending stiffness

A 1D effective bending stiffness is determined by means of standard three-point bending. In order to compare numerical calculations to the experiment, an effective stiffness is extracted from the stiffness entries of the classical laminated plate theory (obtained with the RSE). In the following considerations bending of the x-axis is assumed. For the used sample width $w = 28$ mm and distance of outer supports $L = 60$ mm it is convenient to assume that the three-point bending boundary conditions generate a plain strain state in width-direction. Thus, the equivalent bending stiffness becomes [1]

$$D_{11}^{*} = D_{11} - B_{11}^{2}/A_{11} \tag{26}$$

where the latter part accounts for the discrepancy $\Delta z_{\text{ea}} = -B_{11}/A_{11}$ between the reference plane and the actual location of the elastic neutral plane for bending of the x-axis. The effective bending modulus is then calculated as

$$E^{*} = D_{11}^{*}\frac{12}{(2h)^3}. \tag{27}$$

Note, that there are two additional (but generally different) elastic neutral planes for which the curvatures κ_{yy} and κ_{xy} maintain zero for pure in-plane loads n_{yy} and n_{xy}, respectively.

4. Calculations

This section regards the tested laminate configuration (E-glass-fibre/epoxy $[90,0]_s$) already characterised in Section 3.1. In the following, results are presented which illustrate some theoretical formulations given in Section 2. The following assumptions regarding the RSE finite element model hold:

- There only exist transverse cracks at the bending tension side.
- Cracks extend over the whole thickness of the 90°-ply.
- The crack spacing is uniform.
- The crack-density is only modelled by means of complete and straight cracks, hence $\rho = \bar{\rho}_{\text{RSE}}$, cp. Eq. (24).

A typical mesh of the RSE is shown in Fig. 6 representing a crack-density of $\bar{\rho}_{\text{RSE}} = 800\ \text{m}^{-1}$. Mesh convergence has been proven in terms of macroscopic stiffness output. The unit-cell always includes two cracks while the length l is adjusted to achieve the desired crack-density. The width b is chosen always equal to l and the laminate thickness $2h = 1.68$ mm results from the ply-thickness $t_{\text{ply}} = 0.42$ mm.

Fig. 7 shows contour plots of the six loadcases. As expected, the stress field shows in-plane periodic behaviour. Especially the two loadcases in x-direction (pure n_{xx} and m_{xx} load) are interesting when comparing RSE results to the bending experiment (Section 5). In all cases the crack surfaces are stress-free and the stresses continuously rise with increasing distances from a crack. In case that cracks are not closed (no contact of crack-surfaces), the classical

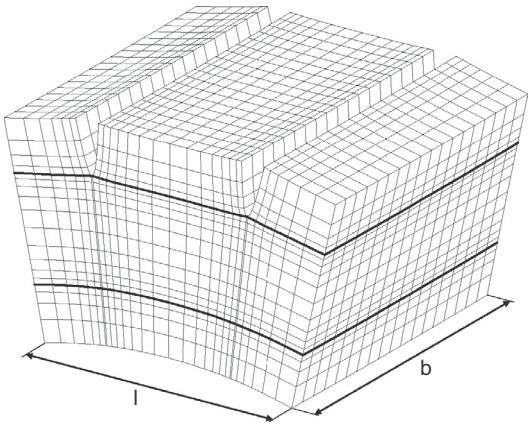

Fig. 6. Typical RSE mesh. The bold lines indicate the borders between the outer 90° and centred 0°-layers.

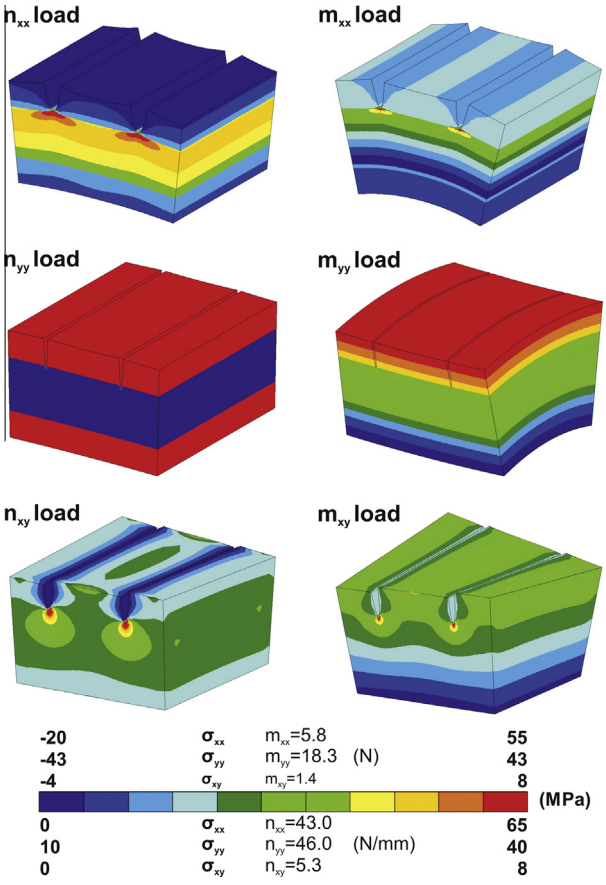

Fig. 7. Contour plot of the six loadcases for $\bar{\rho} = 800\ \text{m}^{-1}$ (exaggerated deformation). The legend shows the load with the associated dominant direct stress components separately for each loadcase. (For interpretation of the references to colour in this figure legend, the reader is referred to the web version of this article.)

laminated plate stiffness matrix of this scenario ($[90,0]_s$ with single-sided cracked 90°-ply) denotes

$$\mathbf{ABD}^{\text{RSE}} = \begin{bmatrix} A_{11} & A_{12} & 0 & B_{11} & B_{12} & 0 \\ & A_{22} & 0 & B_{21} & B_{22} & 0 \\ & & A_{33} & 0 & 0 & B_{33} \\ & & & D_{11} & D_{12} & 0 \\ & \text{sym.} & & & D_{22} & 0 \\ & & & & & D_{33} \end{bmatrix}. \tag{28}$$

Obviously, there are non-zero **B** matrix entries. Among these, B_{11} is dominant as a significant curvature κ_{xx} occurs due to a pure in-plane load n_{xx} (Fig. 7 (n_{xx} load) and Fig. 8(a)) because normal tension stresses are not transferred via the crack surfaces. The same explanation holds for B_{33} and the in-plane shear stress, see Fig. 7 (n_{xy} load) and Fig. 9. Other non-zero coupling entries result from unequally constrained lateral poisson contractions in the cracked and intact outer plies. Precisely, the ply-stiffness in y-direction (parallel to the cracks) is slightly smaller in the cracked ply as the cracks locally allow lateral contractions.

Figs. 8–10 illustrate the strain/curvature extraction process for a crack-density of $\bar{\rho}_{\mathrm{RSE}} = 800\ \mathrm{m}^{-1}$. The two modelled cracks are located in the unit-cell at $x = \pm 0.625$ mm. Fig. 8 shows the undeformed $\mathbf{X}_{\mathbf{RSE}}$ and deformed $\mathbf{x}_{\mathrm{RSE}}$ finite element nodes of the x-axis. Additionally, the equidistantly distributed points $\mathbf{x}_{\mathrm{equidistant}}$ along the deformed x-axis are plotted. These points are finally used to approximate the global circle and as result obtain the global curvature of the unit-cell. Due to the reduced bending stiffness in x-direction around the cracks, the curvature is elevated at these locations, cp. Fig. 8(a). In contrast, the impact of transverse cracks is low regarding loads in y-direction, cp. Fig. 8(b) showing anticlastic bending of the x-axis due to a pure moment m_{yy}. The calculation of the twisting curvature requests a two-dimensional interpolation of the deformed reference plane. Fig. 9 illustrates the deformed finite element nodes $\mathbf{x}_{\mathrm{RSE}}$ and the two diagonals of equidistant points ($\mathbf{x}_{1,\mathrm{equidistant}}$ and $\mathbf{x}_{2,\mathrm{equidistant}}$) used to approximate the two circles for the subsequent estimation of κ_{xy} via Eq. (17).

A slight perspective of the RSE possibilities is given in Fig. 10. Herein, the local curvature $\kappa_{xx}^{\mathrm{local}}$ is shown together with the mean curvature $\kappa_{xx}^{\mathrm{mean}} = \kappa_{xx}$ for a cracked configuration under pure moment load m_{xx}. For this configuration 114 equidistant points are created along the deformed x-axis and the local curvature is determined via Eqs. (12) and (15) for a chosen evaluation window size

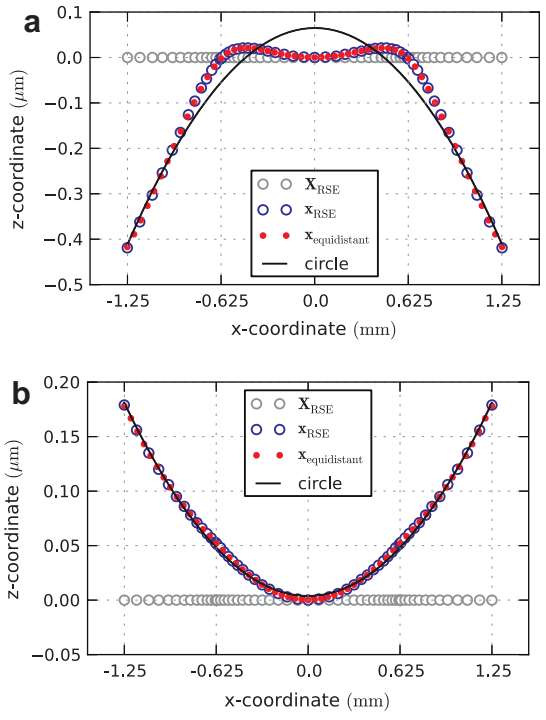

Fig. 8. Extraction of the bending curvature κ_{xx}. The deformed ($\boldsymbol{x}_{\mathrm{RSE}}$) and undeformed ($\boldsymbol{X}_{\mathrm{RSE}}$) x-axis finite element nodes, the equidistant points and the approximated circle are illustrated for a pure in-plane load n_{xx} (a) and moment m_{yy} (b). (For interpretation of the references to colour in this figure legend, the reader is referred to the web version of this article.)

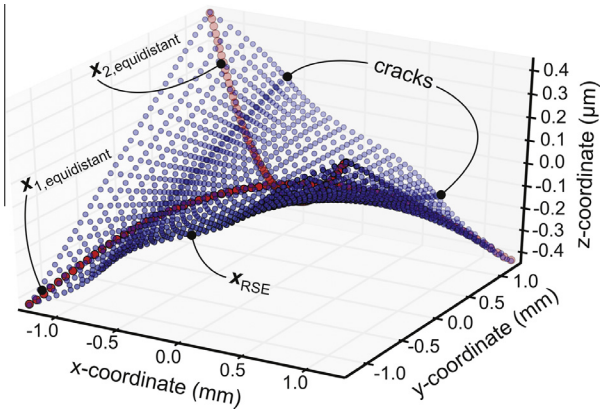

Fig. 9. Extraction of the twist κ_{xy} at the RSE neutral plane. The deformed neutral plane $\boldsymbol{x}_{\mathrm{RSE}}$ and the equidistant diagonal points are visualised for a pure in-plane shear load n_{xy}. (For interpretation of the references to colour in this figure legend, the reader is referred to the web version of this article.)

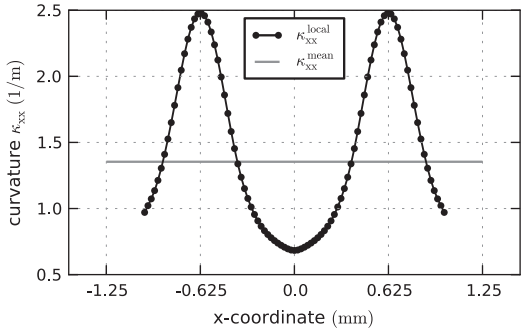

Fig. 10. Local and global x-axis curvature due to a pure m_{xx} moment. Cracks are located at $x = \pm 0.625$ mm.

of 20 connected points. As the evaluation window is always shifted by one point, $\kappa_{xx}^{\mathrm{local}}$ is averaged around 94 locations (each indicated by a dot in Fig. 10) along the x-axis. Note that the finest local resolution corresponds to a minimum of 3 connected points whereas the mean global curvature radius is approximated to all 114 points. In fact, a small evaluation window increases the local resolution but increasing number of points and also evaluation window overlapping enhance the smoothness of the local course. Having this at hand, it can be observed that the local curvature $\kappa_{xx}^{\mathrm{local}}$ reaches maxima at the compliant crack locations and drops below the global curvature $\kappa_{xx}^{\mathrm{mean}}$ in the stiffer intermediate sections.

Next, the dependences of relevant stiffness entries on the crack-density are investigated for the tested laminate configuration. The coupling terms B_{11} and B_{33} are given in Fig. 11(a) using a normalised presentation. As both entries are initially zero and rise with increasing crack-density, the state of maximum investigated damage $\bar{\rho}_{\mathrm{RSE}} = 900\ \mathrm{m}^{-1}$ is chosen as normalisation reference (ABD_{ij}^{0}). Fig. 11(b) shows the entries A_{11}, D_{11}, D_{12} and D_{33}. These entries decrease with increasing crack-density. Hence, the initial value is used for normalisation. As an outer layer is subjected to damage, the impact on bending and coupling is stronger than on in-plane entries. It can be noticed, that all entries tend towards a limit value. Finally, the movement of the elastic neutral plane (axis for which κ_{xx} remains zero for a pure n_{xx} load) Δz_{ea} as a result of transverse cracking is presented in Fig. 12. It is expressed in fractions of the half-thickness $\Delta z_{ea}/h$ meaning that the elastic plane coincides with the reference plane for a value of 0% and with the sample top/bottom for a value of ±100%, respectively.

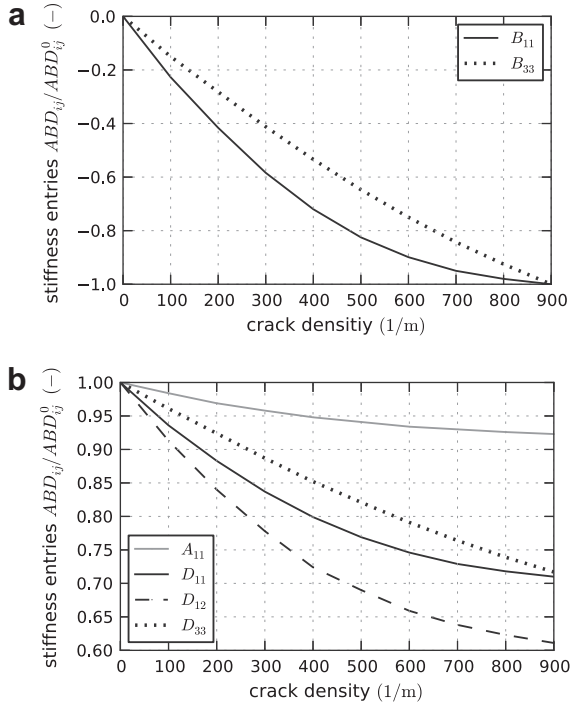

Fig. 11. Relevant normalised classical laminated plate theory stiffness entries against crack-density.

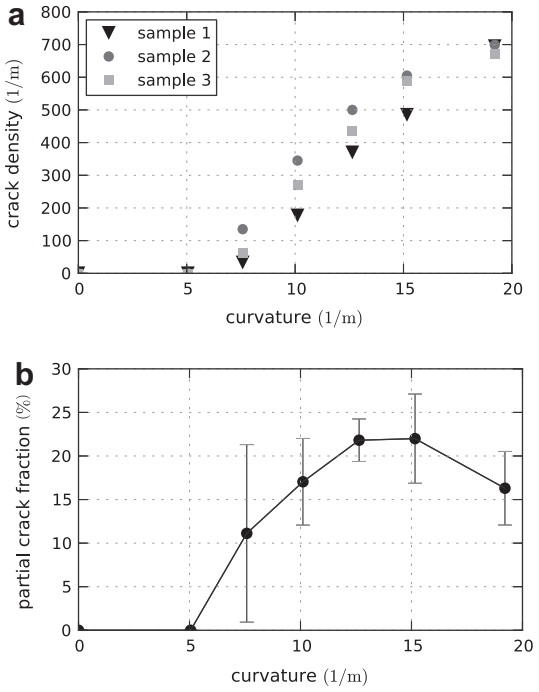

Fig. 13. Measured total (a) and partial (b) crack-density against curvature.

5. Results

This section compares numerical RSE solutions with the conducted bending experiments in terms of static stiffness degradation due to transverse cracks.

Cracks at the pressure side and delamination could never be observed which fully conforms the modelling assumption of one-sided transverse cracks as single damage. For the evaluation of the crack-density all cracks within the damage-zone L are considered. The recorded crack-density is plotted against the curvature, see Fig. 13(a), and the corresponding partial crack fraction $\rho_{\text{partial}}/\rho$ is plotted in Fig. 13(b). Reduced crack development at high loads, which is well-known for in-plane tension, can be observed for these bending experiments, too. A noticeable discrepancy between model and experiment is present in terms of the existence of partial cracks. The partial crack fraction increases until a plateau and finally decreases at high curvatures. This course and the high standard deviation at low curvatures can be explained with the discussed crack initiation pattern (Section 3.3). Most cracks are initiated at the free edges and grow inside the sample. When crack saturation is reached at the sample edges, the crack-density only rises due to expanding, already available partial cracks. Hence, the partial crack-density fraction decreases again at high load levels when most partial cracks have grown across the whole sample width, thus becoming complete cracks. Having in mind that ρ_{partial} is about 20% of the whole crack-density at it's plateau, discrepancies with the model might be expected. On the other hand, remind the two meeting partial cracks in Fig. 5. After the crack-tips have been passed each other, a noticeable slower crack growth is observed. These cracks are still counted as partial cracks but mechanically should almost respond like one straight crack. This is confirmed by the comparison of the numerical and experimental bending stiffness, see Fig. 14. Herein, the three-point normalised bending stiffness is plotted against the recorded crack-density ρ together with the numerical bending stiffness (eq. (27)) against the equivalent model crack-density $\bar{\rho}_{\text{RSE}}$. Obviously, the RSE models the stiffness degradation very well for the entire crack-density range (continuous line). This result confirms the RSE formulation and, additionally, in this case shows the minor impact of the crack topology regarding the global mechanical response. The influence on bending stiffness due to the movement of the elastic axis is also illustrated in Fig. 14. The dotted line

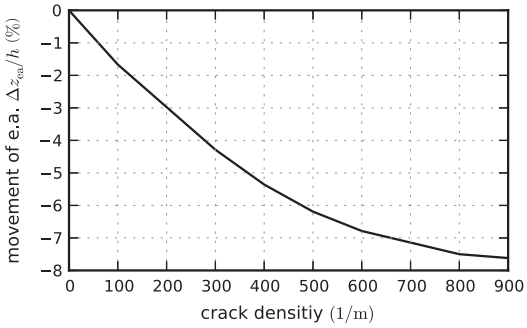

Fig. 12. Movement of the elastic x-axis against crack-density.

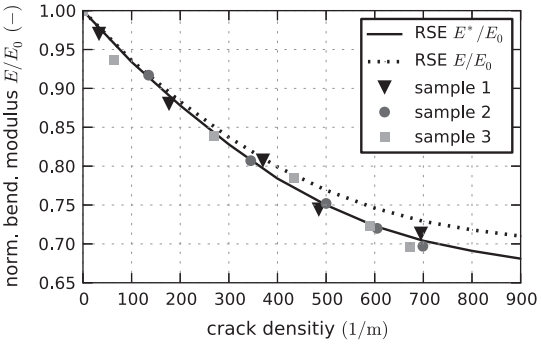

Fig. 14. Measured and calculated normalised bending modulus against crack-density.

represents the bending stiffness which is directly calculated from the D_{11} entry via Eq. (27). This implies that especially at high crack-densities the movement of the elastic neutral planes should be taken into account.

6. Conclusions

This paper presents an unit-cell based homogenisation approach which is settled within the finite element framework and, for the first time, is able to extract all stiffness entries of the classical laminated plate theory. Large heterogeneities or damages like cracks and delaminations can directly be incorporated and representative stiffness properties extracted. Additionally, in contrast to other formulations, it is also possible to generate a pure bending moment loading condition as the locations of the elastic neutral planes are not needed in advance.

In order to validate first numerical results, new bending experiments with E-glass-fibre/epoxy cross-ply laminate are conducted. Herein, transverse cracks were generated by subjecting samples to an almost pure bending state up to curvatures of 20 m^{-1}. The measured bending stiffness degradation due to transverse cracks at the bending tension side agrees well with the numerical predictions for all crack-densities.

Acknowledgement

This work has been funded by the German Science Foundation (DFG) within the the special research field 880 (SFB 880).

References

[1] Kaw AK. Mechanics of composite materials. CRC Press; 2006.
[2] Reddy JN. Mechanics of laminated composite plates and shells: theory and analysis. CRC Press; 2004.
[3] Thomsen OT. Modeling of multi-layer sandwich type structures using a high-order plate formulation. J Sand Struct Mater 2000;2:331–49.
[4] Olympio KR, Gandhi F. Zero poissons ratio cellular honeycombs for flex skins undergoing one-dimensional morphing. J Intell Mater Syst Struct 2009;0:1–17.
[5] Olympio KR, Gandhi F. Flexible skins for morphing aircraft using cellular honeycomb cores. J Intell Mater Syst Struct 2010;21:1719–35.
[6] Xia Y, Friswell MI, Flores EIS. Equivalent models of corrugated panels. Int J Solids Struct 2012;49:1453–62.
[7] Kress G, Winkler M. Corrugated laminate homogenization model. Compos Struct 2010;92:795–810.
[8] Nemat-Nasser S, Hori M. Micromechanics: overall properties of heterogeneous materials. Elsevier; 1999.
[9] Terada K, Hori M, Kyoya T, Kikuchi N. Simulation of the multi-scale convergence in computational homogenization approaches. Int J Solids Struct 2000;37:2285–311.
[10] Ilic S, Hackl K. Application of the multiscale FEM to the modeling of nonlinear multiphase materials. J Theor Appl Mech 2009;47:537–51.
[11] Kouznetsova V, Geers MGD, Brekelmans WAM. Multi-scale constitutive modelling of heterogeneous materials with a gradient-enhanced computational homogenization scheme. Int J Numer Meth Eng 2002;54:1235–60.
[12] Coenen EWC, Kouznetsova VG, Geers MGD. Computational homogenization for heterogeneous thin sheets. Int J Numer Meth Eng 2010;83:1180–205.
[13] Sun C, Vaidya RS. Prediction of composite properties from a representative volume element. Compos Sci Technol 1996;56:171–9.
[14] Garnich MR, Karami G. Finite element micromechanics for stiffness and strength of wavy fiber composites. J Compos Mater 2004;38:273–92.
[15] Karami G, Garnich M. Effective moduli and failure considerations for composites with periodic fiber waviness. Compos Struct 2005;67:461–75.
[16] Adden S, Horst P. Stiffness degradation under fatigue in multiaxially loaded non-crimped-fabrics. Int J Fatigue 2010;32:108–22.
[17] Jiang WG. A concise finite element model for pure bending analysis of simple wire strand. Int J Mech Sci 2012;54:69–73.
[18] Ju F, Xia Z, Zhou C. Repeated unit cell (RUC) approach for pure bending analysis of coronary stents. Comput Methods Biomech Biomed Eng 2008;11:419–31.
[19] Talreja R. Transverse cracking and stiffness reduction in composite laminates. J Compos Mater 1985;19:355–75.
[20] Berthelot JM. Transverse cracking and delamination in cross-ply glass-fiber and carbon-fiber reinforced plastic laminates: Static and fatigue loading. Appl Mech Rev 2003;56:111–47.
[21] McCartney LN, Pierse C. Stress transfer mechanics for multiple ply laminates subject to bending. NPL Rep CMMT(A); 1997. p. 55.
[22] Smith PA, Ogin SL. On transverse matrix cracking in cross-ply laminates loaded in simple bending. Compos Appl Sci Manuf 1999;30:1003–8.
[23] Zhang D, Ye J, Lam D. Ply cracking and stiffness degradation in cross-ply laminates under biaxial extension, bending and thermal loading. Compos Struct 2006;75:121–31.
[24] Li S, Zou Z. The use of central reflection in the formulation of unit cells for micromechanical FEA. Mech Mater 2011;43:824–34.
[25] Kecman V. Learning and soft computing. MIT Press; 2001.
[26] Buhmann MD. Radial basis functions: theory and implementations. Cambridge University Press; 2003.
[27] Gander W, Golub GH, Strebel R. Least-squares fitting of circles and ellipses. BIT 1994;34:558–78.
[28] Chernov NI, Ososkov GA. Effective algorithms for circle fitting. Comput Phys Commun 1984;33:329–33.
[29] Chernov N, Lesort C. Least squares fitting of circles. J Math Imaging Vis 2005;23:239–52.
[30] Karimäki V. Effective circle fitting for particle trajectories. Nucl Instrum Methods 1991;A305:187–91.
[31] Glavonjić M. Circles and ellipses fitting to measured data. FME Trans 2007;35:165–72.
[32] VDI2014, A. Design and construction of fibre reinforced plastics components – basics. VDI; 1989.
[33] Schmitz A, Horst P. Bending deformation limits of corrugated unidirectionally reinforced composites. Compos Struct 2014;107:103–11.
[34] Boers SHA, Geers MGD, Kouznetsova VG. Contactless and frictionless pure bending. Exp Mech 2010;50:683–93.
[35] Yoshida F, Urabe M, Toropov VV. Identification of material parameters in constitutive model for sheet metals from cyclic bending tests. Int J Mech Sci 1997;40:237–49.
[36] Ladevèze P, Lubineau G, Violeau D. A computational damage micromodel of laminated composites. Int J Fract 2006;137:139–50.
[37] Manders PW, Chou TW. Statistical analysis of multiple fracture in 0/90/0 glass fibre/epoxy resin laminates. J Mater Sci 1983;18:2876–89.
[38] Berthelot JM, Corre JFL. Statistical analysis of the progression of transverse cracking and delamination in cross-ply laminates. Compos Sci Technol 2000;60:2659–69.
[39] Berthelot JM, Mahi AE, Corre JFL. Development of transverse cracking in cross-ply laminates during fatigue tests. Compos Sci Technol 2001;61:1711–21.